IEEE INSTRUMENTATION & MEASUREMENT SOCIETY

Received 20 September 2022; revised 18 October 2022; accepted 20 October 2022. Date of publication 15 November 2022; date of current version 8 December 2022. The review of this article was arranged by Associate Editor Samir Trabelsi.

Digital Object Identifier 10.1109/OJIM.2022.3221330

Local Sensitivity Analysis and Monte Carlo Simulation to Examine the Effects of Chipless RFID Measurement Uncertainties—Part II: Consideration of Multiple Measurement Uncertainties

KATELYN BRINKER (Graduate Student Member, IEEE), AND REZA ZOUGHI (Fellow, IEEE)

Center for Nondestructive Evaluation and Department of Electrical and Computer Engineering, Iowa State University, Ames, IA 50014, USA

CORRESPONDING AUTHOR: K. BRINKER (e-mail: brinker@iastate.edu)

ABSTRACT Measurement and response decoding is an ongoing challenge in the chipless radio-frequency identification (RFID) field. Measurement uncertainties, including tag/reader misalignment, S-parameter error, and clutter, can cause response distortions, such as magnitude changes and resonant frequency shifts, that can lead to the improper assignment of a binary code or sensing parameter (i.e., decoding). This work aims to use local sensitivity analysis and Monte Carlo simulation to fully characterize the effects of misalignment, response parameter measurement error (e.g., VNA S-parameter error), and clutter on chipless RFID responses that are measured in the near-field with a monostatic setup. From this type of comprehensive characterization, conclusions are drawn about the identification (ID) and sensing capabilities of the tags. While the effect of misalignment-based uncertainty was examined in Part I, here in Part II, S_{11} uncertainty and clutter-based uncertainty are examined both individually and in combination with misalignment-based uncertainty. An example, demonstrating the application of the proposed tag performance assessment framework is also provided.

INDEX TERMS Chipless radio-frequency identification (RFID), local sensitivity analysis, measurement uncertainty, Monte Carlo analysis.

I. INTRODUCTION

PART I examined the effects of misalignment-based measurement uncertainty on chipless radio-frequency identification (RFID) tag performance through local sensitivity analysis and Monte Carlo simulation. This analysis was done for two different tags and two different coding methods, which are also used here for continuity. It was seen that while local sensitivity analysis can provide insight into the types of misalignment that most important to control for during measurement, Monte Carlo analysis is necessary to fully characterize the effects of misalignment on tag performance [1].

Since misalignments, clutter, and S_{11} error are all measurement uncertainties that can affect decoding performance, this work aims to extend the work in Part I by quantify the effects of all of these factors (both individually and in combination with each other) using Monte Carlo simulation. The simulation results are verified through measurement, and the performance across simulation and measurement is evaluated in terms of metrics such as detection error rate (DER), bit error ratio (BER), resonant frequency, and bit differences. In performing this work, a framework is provided for evaluating the effects of measurement uncertainty on chipless RFID tag responses that can be applied to other tag designs and measurement setups used for both identification and sensing applications.

Here, in Part II, Section II contains the Monte Carlo simulations for S_{11} uncertainty, clutter-based uncertainty, and the combination of these uncertainties with misalignment-based uncertainty. Section III presents measurement results in order

to corroborate the simulation results. Finally, Section IV provides a demonstration of the proposed tag performance assessment framework that has been developed across Part I and Part II.

II. MONTE CARLO SIMULATION

In this section, the effects of S_{11} and clutter-based uncertainty are examined at first individually and then in combination with misalignment-based uncertainty, which was presented in Part I. The same two tags (circular patch and 4C) from Part I are used again here with the same two coding methods (Method 1 and Method 2) and coding method configurations.

A. S_{11} UNCERTAINTY

In continuing the measurement uncertainty-based Monte Carlo analysis presented in Part I, S_{11} uncertainty is next examined. S_{11} uncertainty is a function of the reader used (an Anritsu MS46131A VNA in this case), the cable type and length, the calibration kit and procedure, and the averaging and intermediate frequency bandwidth (IFBW) VNA settings used for the measurements. The averaging and IFBW settings can be manipulated to lower the noise floor at the cost of measurement time, with a lower IFBW and higher averaging corresponding to a lower noise floor. The noise floor in turn plays a role in establishing the achievable signal-to-noise ratio (SNR) for a given measurement configuration. The noise floor along with the calibration procedure determine the test port characteristics of directivity, source match, and load match. These measurement system characteristics are uncertainties which can be propagated to determine the overall S_{11} magnitude and phase uncertainty for a given measurement frequency and S_{11} magnitude [2], [3], [4], [5].

For this work, the Anritsu Exact Uncertainty software was used to perform the uncertainty propagation and generate S_{11} uncertainty curves over the X-band (8.2–12.4 GHz) frequency range for an IFBW of 1 kHz with three times averaging. These IFBW and averaging settings match those used for the measurements that are discussed later in this article. Since waveguide-based calibration options are not provided in the software, a short, open, load connector-based calibration kit was selected. While this is not completely representative of the measurement configuration used in this particular work, it can still be used to provide insight into the effects of S_{11} uncertainty on chipless RFID response decoding [2]. The S_{11} magnitude uncertainty curves for three frequencies throughout the X-band (8.2–12.4 GHz) are shown in Fig. 1. The phase uncertainty curves are not provided here since only the tag's S_{11} magnitude is used in the coding methods that have been selected for this work. However, they could easily be generated and employed if this framework were to be applied to a scenario that did use a phase-based coding method. As can be seen from Fig. 1, the lower the measured S_{11} magnitude, or in other words, the closer the S_{11} magnitude is to the noise floor, the greater the uncertainty. Additionally, as the frequency increases for the given measurement configuration so does the uncertainty, albeit slightly, for each measured S_{11} magnitude. It should also be noted that the Anritsu Exact Uncertainty software used takes a conservative approach to uncertainty propagation (i.e., it overestimates the S_{11} uncertainty) and as a result, all measurements should have less error than that predicted by the results in Fig. 1 [2]. Thus, the subsequent results represent possible "worst-case" scenarios in terms of the effects of S_{11} uncertainty on decoding capabilities.

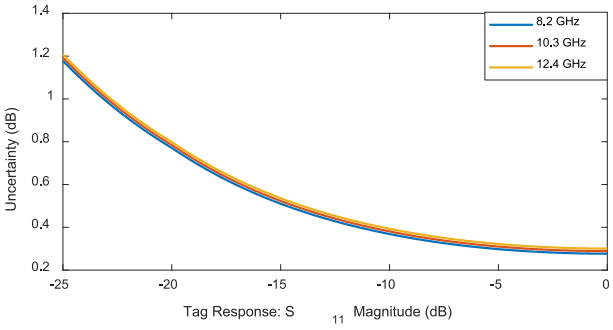

FIGURE 1. Generated S_{11} uncertainty curves using the Anritsu Exact Uncertainty program.

In order to assess the consequences of S_{11} uncertainty on decoding capabilities, another Monte Carlo simulation using 100 000 trials was conducted. For this simulation, the simulated responses of the patch and 4C tags with no misalignments were used. For each trial, the tag response was adjusted one frequency point at a time with an offset generated based on the S_{11} uncertainty given by the 12.4-GHz curve in Fig. 1. This 12.4-GHz curve was used to provide additional conservativeness to the results. The offset was generated by creating a random variable using a normal distribution with the mean set to zero and the standard deviation set to the uncertainty in Fig. 1 that corresponds to the tag response magnitude at the frequency point under consideration. For example, for the patch tag, the magnitude at the resonant frequency of 10.38 GHz is −18.19 dB, which corresponds to an S_{11} uncertainty of 0.686 dB when using the 12.4-GHz curve. Therefore, an offset for the tag response at 10.38 GHz would be generated by creating a random variable with a normal distribution with a mean of 0 and a standard deviation of 0.686 and adding it to the response at 10.38 GHz.

After each frequency point in the tag response was adjusted with S_{11} uncertainty, the response was coded using the different coding methods discussed in Part I. From these results over the 100 000 trials, cumulative distribution function (CDF) curves were generated and used to compare the different coding methods. A flowchart depicting the procedure for this Monte Carlo simulation is shown in Fig. 2, while the results for the patch and 4C tag responses with and without S_{11} uncertainty are shown in Fig. 3(a) and (b), respectively. The results show greater uncertainty

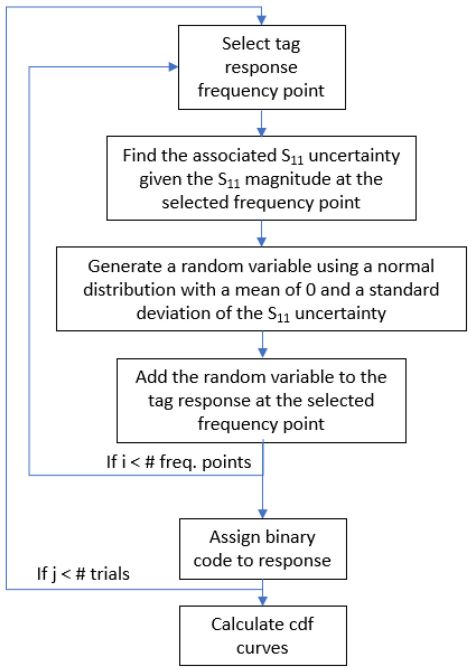

FIGURE 2. Flowchart for S_{11} uncertainty Monte Carlo simulation.

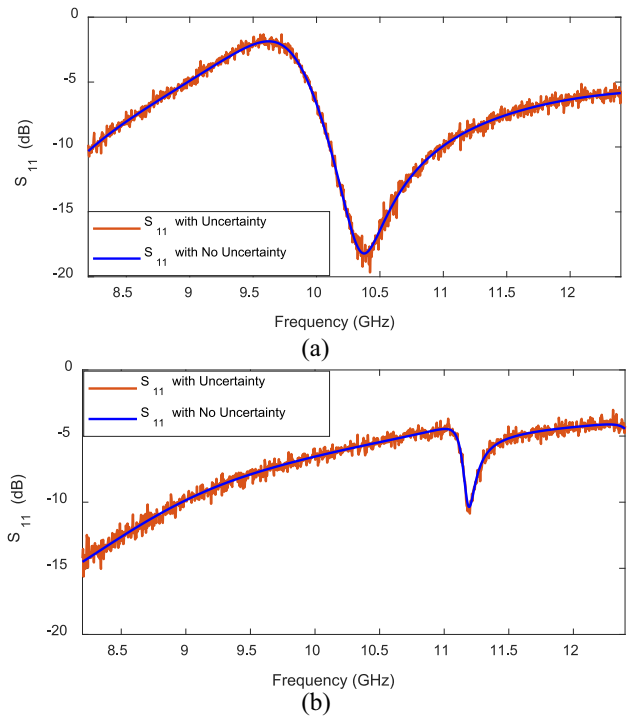

FIGURE 3. Examining the effect of S_{11} uncertainty on tag responses with no misalignment: (a) patch tag response with S_{11} uncertainty and (b) 4C with S_{11} uncertainty.

for lower S_{11} magnitudes as expected from the curves in Fig. 1.

One must note that all curves in Fig. 3 are simulated results. The S_{11} with no uncertainty curves are the "idealized" curves that come directly from CST Studio Suite®, where there is effectively no noise and a very high dynamic range.

TABLE 1. Decoding metrics given S_{11} uncertainty.

Coding Method	Average BER	DER	Throughput
Circular Patch Tag			
Method 1: t=-1 dB, 25 bits	6.5%	100.0%	0.0%
Method 1: t=-3 dB, 25 bits	1.0%	26.0%	74.0%
Method 1: t=-5 dB, 25 bits	9.8%	100.0%	0.0%
Method 1: t=-1 dB, 52 bits	5.4%	100.0%	0.0%
Method 1: t=-3 dB, 52 bits	4.5%	100.0%	0.0%
Method 1: t=-5 dB, 52 bits	13.0%	100.0%	0.0%
Method 2: t=-1 dB	0.0%	0.0%	100.0%
Method 2: t=-5 dB	5.0%	5.0%	95.0%
Method 2: t=-10 dB	5.0%	5.0%	95.0%
Method 2: t=-15 dB	5.0%	1.1%	98.9%
4C Tag			
Method 1: t=-1 dB, 25 bits	16.6%	100.0%	0.0%
Method 1: t=-3 dB, 25 bits	12.5%	100.0%	0.0%
Method 1: t=-5 dB, 25 bits	3.9%	95.7%	4.3%
Method 1: t=-1 dB, 52 bits	18.3%	100.0%	0.0%
Method 1: t=-3 dB, 52 bits	6.7%	100.0%	0.0%
Method 1: t=-5 dB, 52 bits	4.7%	100.0%	0.0%
Method 2: t=-1 dB	0.4%	0.4%	99.6%
Method 2: t=-5 dB	0.1%	0.1%	99.9%
Method 2: t=-10 dB	0.0%	0.0%	100.0%
Method 2: t=-15 dB	0.0%	0.0%	100.0%

The S_{11} with uncertainty curves are what result when the simulated curves from CST Studio Suite® have uncertainty added to them. Due to the conservativeness of the uncertainty propagation model, the uncertainties depicted in Fig. 1 and, therefore, the S_{11} with uncertainty curves in Fig. 3, represent a possible worst case scenario of the potential S_{11} error that would be present with VNA calibration.

Fig. 4 depicts the CDFs of bit differences for each coding method for each tag given S_{11} uncertainty. The number of bit differences was calculated by comparing the coded tag responses with S_{11} uncertainty to the coded tag response without S_{11} uncertainty. In all cases, there was no tag/reader misalignment considered. In the legend in Fig. 4, t represents the threshold used in the coding method, while n represents the number of bits in the code. Each curve in Fig. 4 has a discretized nature due to the number of bit differences being an integer (i.e., fractional bit differences are not possible) and each curve describes the probability of having a certain number of bit differences or fewer. For example, Fig. 4(a) shows that for the patch tag when Method 1 is used for coding with a threshold of -3 dB and a code length of 52 bits, there is a 64.72% chance of having two or fewer bit differences. Fig. 4(b), on the other hand, shows that for Method 2 thresholds of -5 or -10 dB, there is a 95% chance of there being no bit differences.

From these results depicted in Fig. 4, the BER per trial, the average BER for all 100 000 trials, DER, and throughput can also be calculated. Definitions for these metrics are provided in Part I. These metrics are reported in Table 1 for each coding method and for each tag. It should be noted that resonant frequency variability is not used as a metric in this case, due to S_{11} uncertainty mainly affecting the magnitude of the response.

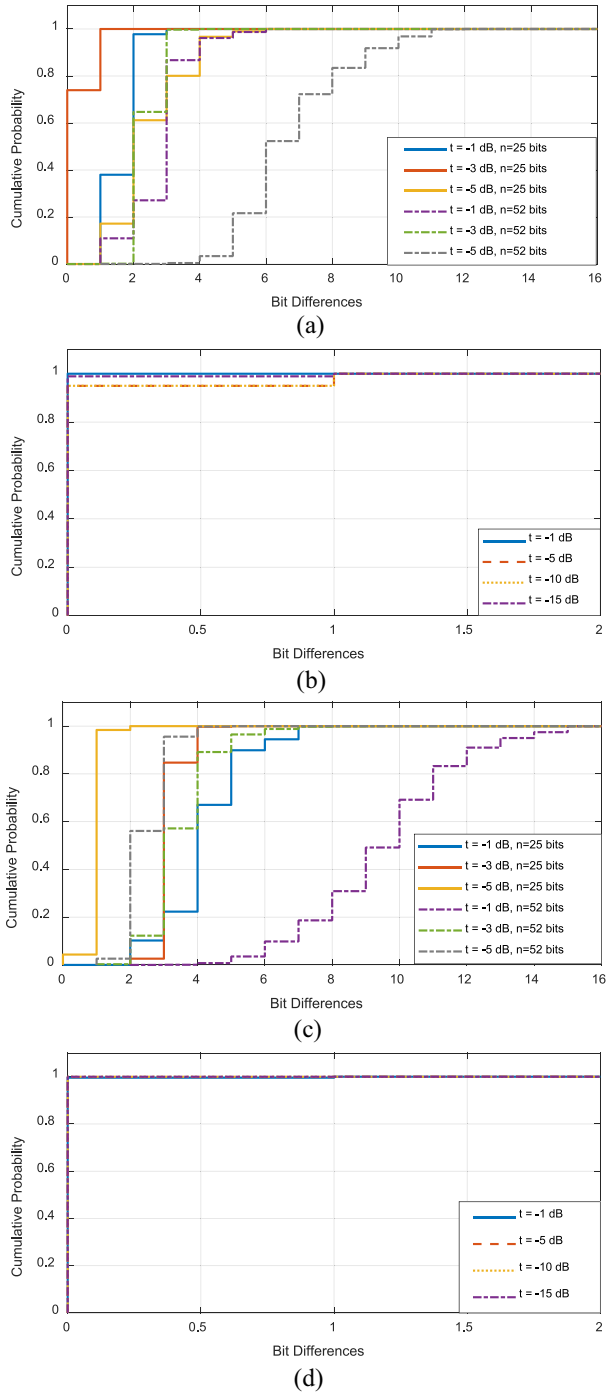

FIGURE 4. Cumulative probability distribution of bit differences when S_{11} uncertainty is considered with different coding methods: (a) CDFs for the patch tag with coding method 1, (b) CDFs for the patch tag with coding method 2, (c) CDFs for the 4C tag with coding method 1, and (d) CDFs for the 4C tag with coding method 2.

B. CLUTTER UNCERTAINTY

The consequences of clutter from the measurement environment (i.e., background reflections and multipath) can also be analyzed using Monte Carlo simulation. For this purpose, a multipath Rician fading channel model, which is designed for line-of-sight communication purposes, is used rather than an additive white or colored noise model. The reason for this is that white noise is more representative of the receiver noise, which is already accounted for in the S_{11} uncertainty analysis of the previous section, than background reflections [3]. When it comes to colored noise, Brownian noise has been previously used in chipless RFID Monte Carlo simulations to mimic the effects of tag movement [6]. However, the measurement configuration used in this work is static so this is also not applicable. A Rician channel model has been previously employed with Monte Carlo simulation in [7] and [8] for chipless RFID systems to assess the BER as a function of the transmit-power to clutter-power ratio for a reading distance of 50 cm and a correlation function-based coding method. Since this work considers a tag measured in the near-field of a "reader," a modified Rician channel model is utilized in the subsequent Monte Carlo simulations. In this case, the coding is performed with Methods 1 and 2 in order to directly compare the effects of clutter with the other measurement uncertainties assessed in this work.

In a Rician channel model, the user can select an appropriate mean channel gain, maximum doppler shift, and a K factor to model the scenario, which, in this case, is a stationary near-field monostatic chipless RFID measurement configuration. As such, the maximum doppler shift has been set to 0 and the mean channel gain has been set to -52.6 dB to be in line with the indoor clutter channel characterization for UWB passive RFID tags that was determined in [9]. The K factor represents the ratio of the direct path signal power to the indirect path signal power and can be estimated from measured tag responses with the following relationship [10], [11]:

$$\frac{E[A]}{\sqrt{E[A^2]}} = \sqrt{\frac{\pi}{4K+4}} e^{(-K/2)} * \left[(K+1) I_0\left(\frac{K}{2}\right) + K I_1\left(\frac{K}{2}\right) \right]. \tag{1}$$

In (1), $E[A]$ represents the average amplitude of the measured signal (S_{11}), $E[A^2]$ represents the average of the amplitude squared, I_o is the zeroth-order modified Bessel function of the first kind, and I_1 is the first-order modified Bessel function of the first kind. In order to estimate K, the left-hand side of (1) was calculated by considering 289 measurements conducted with the measurement configuration depicted in Fig. 5. Fig. 5 shows the X-band (8.2–12.4 GHz) rectangular waveguide with an engineered flange connected to a VNA and attached to multiple rotational stages and an XY scan table. The tag was placed on pieces of low scattering green foam with a low relative permittivity of ∼1.1. The VNA was calibrated up to the waveguide flange aperture. To get the 289 measurements, the rotational stages were set so that the waveguide was not intentionally tilted relative to the tag, the standoff distance was set to 10 mm, and an 8 mm by 8 mm XY scan with a step size of 0.5 mm was conducted. The amplitudes of the measured responses over this scan area were averaged and an estimator [left-hand side of (1)] was determined. The estimator based on measurement (red curve in Fig. 6) was then compared to the right-hand side of (1) (blue curve in Fig. 6), which was directly calculated.

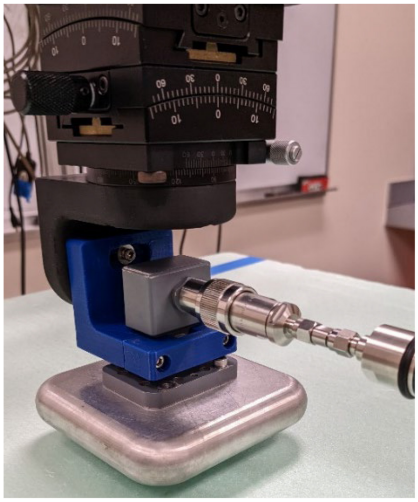

FIGURE 5. Measurement setup for determining the Rician *K* factor.

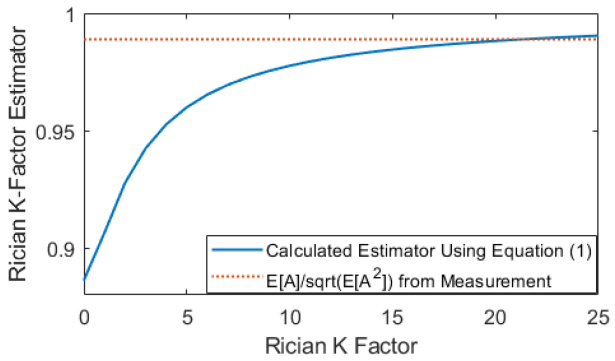

FIGURE 6. Rician *K* factor estimation.

The *K* factor can be estimated by determining the intersection of the two curves in Fig. 6, which in this case is 21. Using this *K* factor of 21, a Rician channel that approximates the measurement environment is created. This relatively high *K* factor means that the direct signal path power is dominant over the power of the indirect signal paths (i.e., the clutter contribution is very low) [10], [11].

Fig. 7 shows the reference response for each tag along with two instances of the reference response being filtered by two instances of the previously described Rician channels. From Fig. 7, the probabilistic nature of the Rician channel (i.e., the channel's amplitude gain is described by a Rician distribution) is demonstrated by the two instances of filtering by the channel being different for each tag [9], [10], [11]. Fig. 7 also shows that the channel mainly has the effect of changing the magnitude of the response. Thus, to assess the consequences of clutter in terms of coding capabilities, Monte Carlo simulation is again employed. The flow chart for the simulation is shown in Fig. 8. This Monte Carlo simulation again uses 100 000 trials, and in each trial, a new Rician channel is generated and used to filter the reference response (i.e., misalignments are not considered in this simulation). The response is then coded using Methods 1 and 2

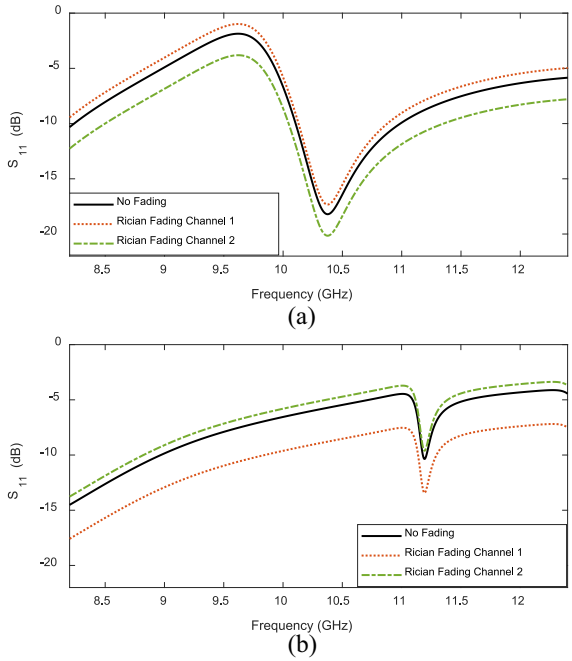

FIGURE 7. Tag responses with and without filtering by a Rician channel: (a) patch tag responses and (b) 4C tag responses.

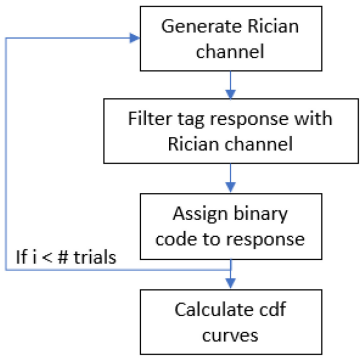

FIGURE 8. Flowchart for clutter uncertainty Monte Carlo simulation.

(see Part I). The CDFs and decoding metrics are reported in Fig. 9 and Table 2, respectively.

From Fig. 9 and Table 2, it can be seen that clutter-based uncertainty for this particular measurement setup (i.e., near-field monostatic) generally results in low BERs and DERs, with the 4C tag generally having higher BERs and DERs than the patch tag for both coding methods. This is largely due to the fact that the Rician channel tends to change the response magnitude more than resonant frequency characteristics, which is largely corrected for in the response normalization that is performed as part of each coding method. Furthermore, these results are in line with the expectation that for near-field chipless RFID measurements, clutter does not have a large effect on the response. However, if the proposed chipless RFID performance assessment framework was to be applied to a measurement setup with a larger reading distance or scenarios with moving tags, we can expect a more significant clutter influence. In that case, the Rician

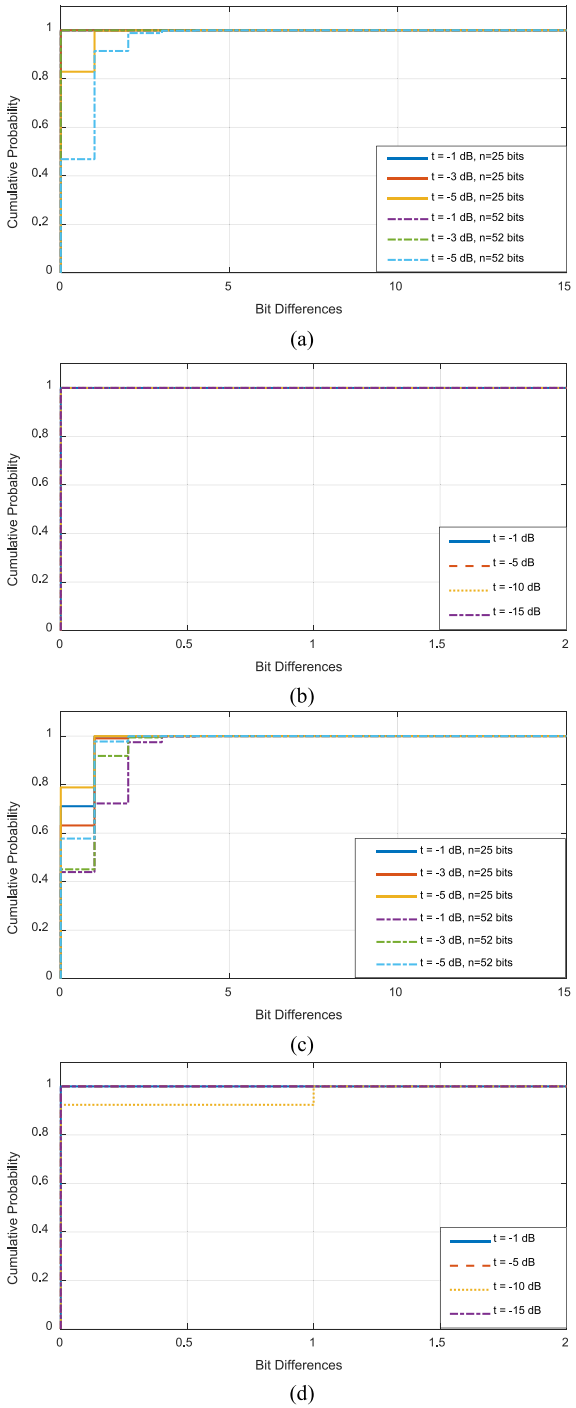

FIGURE 9. Cumulative probability distribution of bit differences when clutter uncertainty is considered with different coding methods: (a) CDFs for the patch tag with coding method 1, (b) CDFs for the patch tag with coding method 2, (c) CDFs for the 4C tag with coding method 1, and (d) CDFs for the 4C tag with coding method 2.

channel model would need to be adjusted accordingly. It should be noted that in practice, chipless RFID reading distances are typically less than 1 m [12]. In terms of other reported BERs in the chipless RFID field, values between 0.001% and 100% have been reported when considering the BER as a function of the transmit power to clutter power ratio [7], [8]. In comparing these results to those for S_{11} uncertainty, it can be seen that S_{11} uncertainty has a larger effect on decoding performance. Since the clutter, similar to S_{11} uncertainty, mainly affects the response magnitude, resonant frequency is again not used as a metric for this simulation.

TABLE 2. Decoding metrics given clutter uncertainty.

Coding Method	Average BER	DER	Throughput
Circular Patch Tag			
Method 1: t=-1 dB, 25 bits	5.2e-4%	0.01%	99.99%
Method 1: t=-3 dB, 25 bits	0.00%	0.00%	100.00%
Method 1: t=-5 dB, 25 bits	0.39%	17.09%	82.91%
Method 1: t=-1 dB, 52 bits	1.15e-4%	0.01%	99.99%
Method 1: t=-3 dB, 52 bits	1.34e-4%	4.0e-3%	99.996%
Method 1: t=-5 dB, 52 bits	1.21%	53.13%	46.87%
Method 2: t=-1 dB	0.00%	0.00%	100.00%
Method 2: t=-5 dB	1.00e-3%	1.00e-3%	99.999%
Method 2: t=-10 dB	0.00%	0.00%	100.00%
Method 2: t=-15 dB	0.00%	0.00%	100.00%
4C Tag			
Method 1: t=-1 dB, 25 bits	1.17%	28.92%	71.08%
Method 1: t=-3 dB, 25 bits	1.52%	36.84%	63.16%
Method 1: t=-5 dB, 25 bits	0.85%	21.15%	78.84%
Method 1: t=-1 dB, 52 bits	1.66%	56.06%	43.94%
Method 1: t=-3 dB, 52 bits	1.22%	54.93%	45.07%
Method 1: t=-5 dB, 52 bits	0.86%	42.25%	57.75%
Method 2: t=-1 dB	0.00%	0.00%	100.00%
Method 2: t=-5 dB	0.00%	0.00%	100.00%
Method 2: t=-10 dB	7.59%	7.59%	92.41%
Method 2: t=-15 dB	0.00%	0.00%	100.00%

Among all three measurement uncertainties examined in Part I and Part II, it can be seen that misalignment-based uncertainty tends to cause the highest bit error and DERs for both coding methods.

C. COMBINING MEASUREMENT UNCERTAINTIES

While the previous sections examined the effects of individual measurement uncertainties, in practice the measurement uncertainties occur simultaneously. To capture the effects of misalignment, S_{11}, and clutter-based uncertainty, a final Monte Carlo simulation was performed. For this simulation, the 1100 cases used in the misalignment study in Part I were again used along with the processes for generating S_{11} uncertainty and clutter uncertainty. For this simulation, after the misalignment case is generated and simulated using CST, the response is passed through a Rician channel and then S_{11} uncertainty is applied through generated offsets as per the process outlined in Part A of this section. The flowchart of the Monte Carlo simulation is shown in Fig. 10.

The CDFs and metrics for this simulation are shown in Fig. 11 and Table 3, respectively. By comparing these results to those in the previous sections, it can be seen that combining all three uncertainties has the effect of increasing the probability of bit differences, the BER, and the DER over the case when just one measurement uncertainty is considered. These results also confirm that misalignment uncertainty is the greatest contributor of the three measurement uncertainties considered to bit differences.

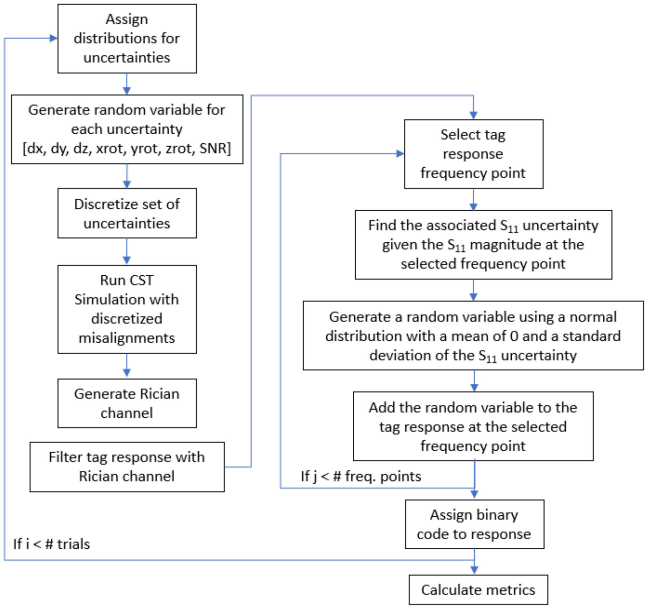

FIGURE 10. Flowchart for the measurement uncertainty Monte Carlo simulation considering misalignment, clutter, and S_{11} uncertainty.

TABLE 3. Decoding metrics considering S_{11}, clutter, and misalignment uncertainties.

Coding Method	Average BER	DER	Throughput
Patch Tag			
Method 1: t=-1 dB, 25 bits	8.12%	100.00%	0.00%
Method 1: t=-3 dB, 25 bits	8.47%	78.55%	21.45%
Method 1: t=-5 dB, 25 bits	22.23%	99.45%	0.55%
Method 1: t=-1 dB, 52 bits	8.08%	99.91%	0.09%
Method 1: t=-3 dB, 52 bits	9.17%	98.64%	1.36%
Method 1: t=-5 dB, 52 bits	22.25%	99.82%	0.18%
Method 2: t=-1 dB	0.00%	0.00%	100.00%
Method 2: t=-5 dB	31.82%	31.82%	68.18%
Method 2: t=-10 dB	4.27%	4.27%	95.73%
Method 2: t=-15 dB	17.91%	17.91%	82.09%
4C Tag			
Method 1: t=-1 dB, 25 bits	16.74%	98.91%	1.09%
Method 1: t=-3 dB, 25 bits	15.87%	99.91%	0.09%
Method 1: t=-5 dB, 25 bits	8.79%	94.82%	5.18%
Method 1: t=-1 dB, 52 bits	18.06%	100.00%	0.00%
Method 1: t=-3 dB, 52 bits	9.18%	97.64%	2.36%
Method 1: t=-5 dB, 52 bits	9.97%	99.45%	0.55%
Method 2: t=-1 dB	1.91%	1.91%	98.09%
Method 2: t=-5 dB	0.00%	0.00%	100.00%
Method 2: t=-10 dB	85.27%	85.27%	14.73%
Method 2: t=-15 dB	0.00%	0.00%	100.00%

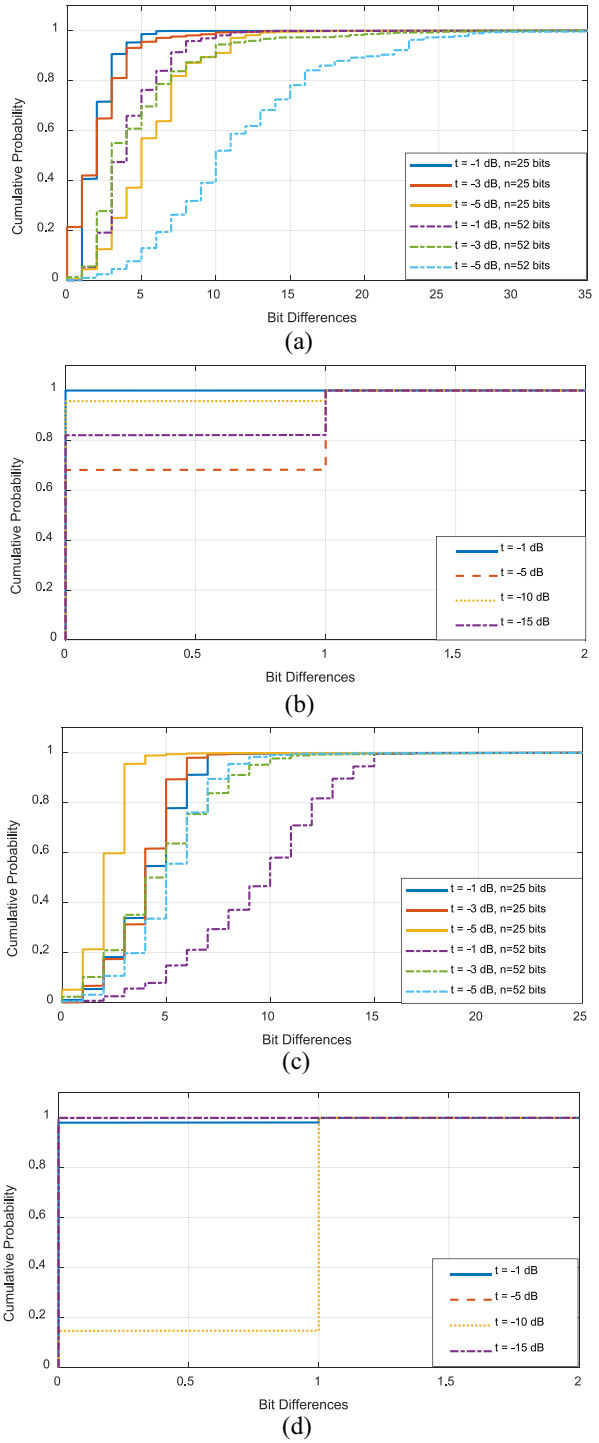

FIGURE 11. Cumulative probability distribution of bit differences when all three measurement uncertainties are considered with different coding methods: (a) CDFs for the patch tag with coding method 1, (b) CDFs for the patch tag with coding method 2, (c) CDFs for the 4C tag with coding method 1, and (d) CDFs for the 4C tag with coding method 2.

Beyond coding-based metrics, the response-based metrics, such as resonant frequency and resonant frequency shift, are also relevant due to the inclusion of misalignment-based uncertainty. To this end, the resonant frequency and the resonant frequency shift as compared to the reference response (aligned with no clutter and no S_{11} uncertainty) resonant frequency were determined at the coding stage of each trial in the Monte Carlo simulation. Just as in Part I, it should be noted that the resonant frequency is not coding-method dependent, so only one set of results is provided for each tag. Fig. 12(a) and (c) shows the histogram of the resonant frequency for each of the 1100 trials and a fitted probability distribution to each. For the patch tag, it was found that a Burr distribution provides the best fit due to the left-skewed nature of the data, while for the 4C tag, it was found

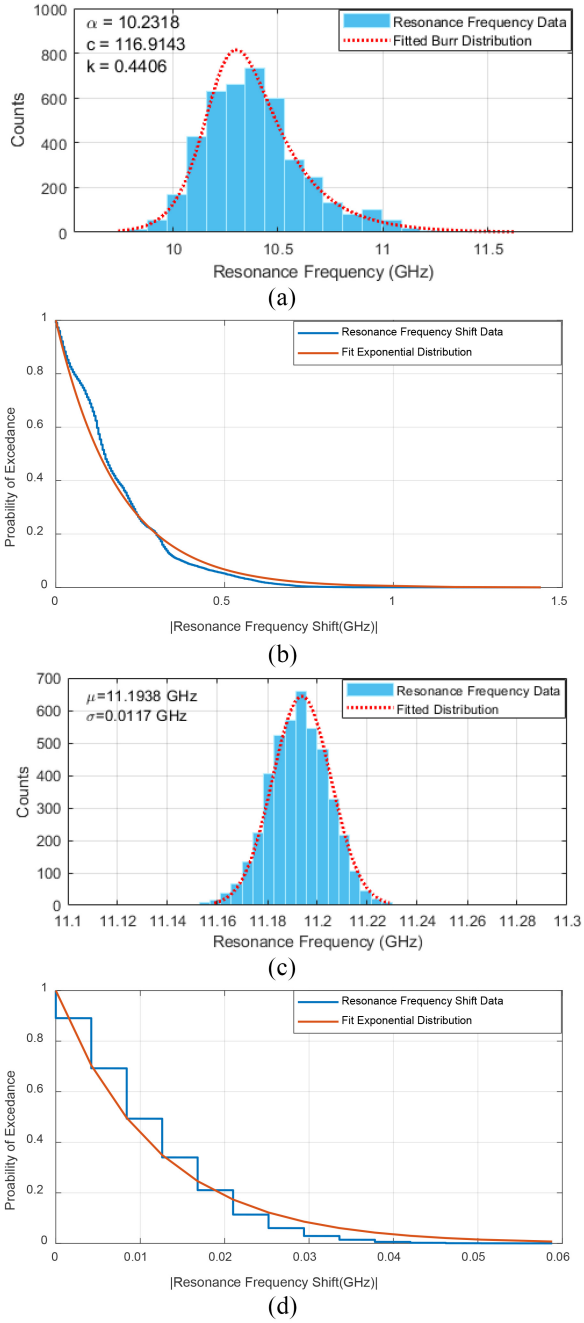

FIGURE 12. Resonant frequency distribution and CDF: (a) patch tag resonant frequency distribution, (b) patch tag resonant frequency shift risk curve, (c) 4C tag resonant frequency distribution, and (d) 4C tag resonant frequency shift risk curve.

that a normal distribution provides the best fit. The resonant frequency for each reference responses is provided in Table 4 for comparison purposes. By comparing Fig. 12(a) and (c) to the resonant frequencies in Table 4, it can be seen that for both cases, the average resonant frequency is not equivalent to the reference.

Next, the magnitude of the resonant frequency shift for each trial for each tag was considered. It was found that for both tags, an exponential distribution could be fit to the magnitude of the resonant frequency shift data. This

TABLE 4. Resonant frequency distributions.

Tag	Ref. Resonant Frequency (GHz)	Average Resonant Frequency (GHz)	95% CI (GHz)	
Patch	10.3840	10.3975	9.9361	10.8589
4C	11.2030	11.1938	11.1704	11.2172

data and the fitted distribution were then used to create risk curves, which are shown in Fig. 12(b) and (d) for the patch tag and 4C tag, respectively. Based on these risk curves, it can be seen that there is a 5% chance of there being a resonant frequency shift magnitude greater than 0.50 GHz for the patch tag and a 5% chance of there being a resonant frequency shift magnitude greater than 0.03 GHz for the 4C tag. In other words, the patch tag is more likely to experience larger resonant frequency shifts than the 4C tag when measurement uncertainty is considered. These findings are supported by the 4C tag resonant frequency data having a smaller spread than that of the patch tag resonant frequency data, which is reported in Table 4 via the 95% confidence interval for each set of resonant frequency data. Another thing to note is that while Fig. 12(d) appears more discretized than Fig. 12(b), this is due to the difference in x-axis limits in the plots, not the resonant frequency behavior of the 4C tag.

These findings can also be used to draw conclusions about the practicality of using each tag for sensing applications. If, for example, a sensing scenario was considered in which the sensing parameter of interest (e.g., dielectric properties or pressure) caused a shift in the resonant frequency, then, each tag would only be able to reliably determine sensing parameter values that correspond to resonant frequencies outside of the expected variability due to measurement uncertainty [13], [14], [15]. This means that the patch tag would have a worse sensing resolution than the 4C tag due to the patch tag having a larger resonant frequency spread and greater risk of resonant frequency shift.

III. MEASUREMENT

In order to corroborate the simulation results in the previous section, a set of measurements was completed with the 4C tag. The fabricated tag and loaded waveguide measurements at X-band (8.2–12.4 GHz) have been previously reported in [1] and [16]. For the measurements used to corroborate the Monte Carlo analysis, an X-band (8.2–12.4 GHz) waveguide with an engineered flange was attached to a set of rotational stages on an XY scanner and the tag was placed below the waveguide aperture at a standoff distance of 10 mm. The waveguide was attached to a VNA and then the system was calibrated up to the waveguide aperture. This measurement setup was the same as the one shown previously in Fig. 5. Scans were then made over an 8 mm × 8 mm area with a step size of 0.5 mm. Due to it being extremely challenging to avoid misalignment (see Part I), the scans were conducted over an area larger

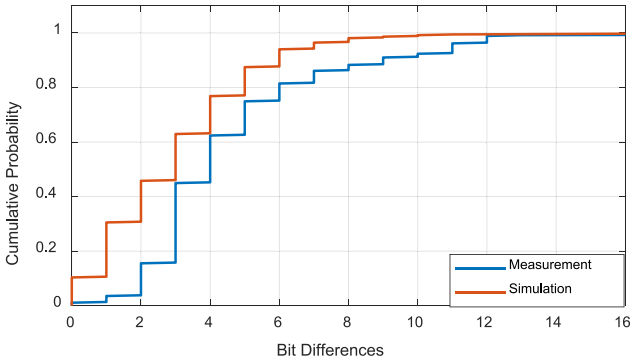

FIGURE 13. Comparison of Monte Carlo analysis for measurement and simulation using the 4C tag.

than that indicated by the probability distributions shown in Part I. This allowed for the reference case to be determined after the measurements were completed by comparing the measured S_{11} in each scan location to simulation with the RMSE calculation shown in Part I. After the reference case was determined, the scan data was cropped so that the reference case was in the center and an equal number of measurements were made in each direction around the center. As an example, if the reference case was found to occur at $dx = -0.5$ mm and $dy = 1$ mm, the scan dataset would cropped to $dx = -3.5$–2.5 mm and $dy = -2$–4 mm so that the reference was in the center. This process allowed misalignment-based uncertainty to be minimized and kept the reference case in the center of the misalignment-based probability distributions. For each scan, the rotational stages were used to create different x-, y-, and z-axis rotations with the following values for a total of 15 scans.

1) *x-Axis Rotations:* $-3°$, $-2°$, $-1°$, $0°$, $1°$, $2°$, and $3°$.
2) *y-Axis Rotations:* $-2°$, $-1°$, $0°$, $1°$, and $2°$.
3) *z-Axis Rotations:* $-2°$, $0°$, $1°$, and $3°$.

It should be noted that only one rotation-based misalignment was used per scan (e.g., x-axis and y-axis rotations did not occur simultaneously). This was primarily due to the extremely time-consuming nature of these measurements.

After the scans were completed and the datasets were cropped, the data was aggregated and coded according to Method 1 using a threshold of -3 dB and a code length of 52 bits. This results in a dataset with 4060 coded responses. Since this measurement data was generated using uniform distributions of each misalignment uncertainty due to the limitations of the equipment, the dataset was randomly sorted and then the first 1100 cases were pulled to generate the CDF shown in Fig. 13. To mimic this measurement process, 1100 simulations were conducted using the process outlined in Fig. 10 with the same misalignments as those as those used in the measurement data. The responses were subsequently coded. The results of this simulation process are shown in Fig. 13 in comparison to the measurement results. The results show that for simulation, there is a greater probability of bit differences being present than there is for measurement. This means that the simulation model is more

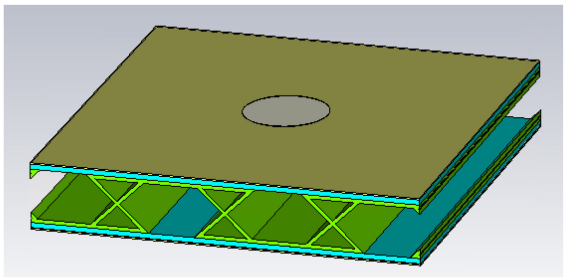

FIGURE 14. CST Studio Suite® model of a pressure sensing tag from [?].

conservative in terms of predicting bit differences than measurement. This makes sense due to the S_{11} uncertainty being generated through a model that will tend to overestimate error. In practice, using this more conservative simulation model will allow for the design of sensing-based tags with a factor of safety built in.

IV. APPLICATION EXAMPLE

In order to demonstrate the utility of this tag performance assessment framework, the performance of a previously published pressure-sensing tag is assessed here [?], [14]. The CST Studio Suite® model of the tag is shown in Fig. 14. As can be seen, this tag also has a circular patch resonator, but its substrate, which is a flexible 3-D printed structure, is heterogeneous and anisotropic. The substrate design allows the tag to compress when it is in the presence of environmental pressure. This changes the substrate height and the effective permittivity of the substrate and, hence, the resonant frequency of the tag. This change in resonant frequency is used to determine the environmental pressure. This tag was chosen because of its similarity to the circular patch tag that was assessed in this work and because it uses a resonant frequency shift sensing approach. The goal of applying the performance assessment framework to this tag is to evaluate the sensing resolution that can be achieved and determine whether a circular patch is a suitable resonator for this application.

The proposed framework that has been developed across Part I and Part II will be applied as follows.

1) Define the measurement setup and the reference case.
2) Determine what measurement uncertainties and misalignment types are relevant based on the measurement setup.
3) Select the appropriate metrics—coding-based metrics, such as BER for identification applications and response characteristic-based metrics like average resonant frequency for sensing applications.
4) Perform a local sensitivity analysis for the relevant types of misalignments and determine which types are the most important to control for.
5) Perform Monte Carlo simulations for the relevant measurement uncertainties.
6) Assess performance based on the resulting metrics.

In terms of step 1 for the selected example, the measurement setup and the reference case are the same as those

presented in this work, namely: measuring S_{11} using an X-band (8.2–12.4 GHz) open-ended waveguide probe with an engineered flange with a 10-mm standoff. The reference case is for a 10-mm standoff with the tag centered on the waveguide aperture and no environmental pressure, which corresponds to a substrate height of 5 mm. For step 2, because S_{11} is being measured in the near-field and misalignments are still possible, all three measurement uncertainties considered in this work are relevant.

Moving on to step 3 of the framework, only response characteristic-based metrics are considered because this tag is intended to be used for a sensing application. As such, average RMSE, average resonant frequency, and average resonant frequency shift could then be relevant for the local sensitivity analysis. These metrics provide insight into which types of misalignment are the most important to be controlled. For the Monte Carlo analysis, the resonant frequency distribution and resonant frequency shift risk curve are the most relevant since it will help determine the achievable sensing resolution. Since the resonant frequency of this tag changes with the applied environmental pressure, it is also desired to perform the local sensitivity analysis and Monte Carlo analysis for multiple pressures corresponding to different substrate heights.

The effects of individual misalignments on the tag response for three different substrate heights (3, 4, and 5 mm) were previously shown in [14] and [?] so they are excluded here for brevity. These results showed that this tag is the most sensitive to *dz* translations, while having no sensitivity to *zrot* rotation and minimal sensitivity to *xrot* and *yrot* rotations. This matches the behavior seen for the Patch tag in Part I, Section II and again indicates that *dz* translations are the most important to control for in the measurement setup.

The next step in the framework would be to perform the Monte Carlo simulations for the considered uncertainties. Since all three uncertainties are relevant for this case, the procedure shown in the flowchart in Fig. 10 is followed, replacing the step of assigning a binary code with recording the resonant frequency. These simulations should be performed for at least the no pressure case (substrate height of 5 mm) and preferably for multiple substrate heights (i.e., different pressures). However, due to the time-consuming nature of the simulations, 200 cases are run for a substrate height of 5 mm. The resulting metrics are therefore illustrative as at least 1100 simulation cases would be needed in order to fully assess the sensors performance. Fig. 15(a) shows the resonant frequency distribution for a substrate height of 5 mm when all three measurement uncertainties are considered, while Fig. 15(b) shows the risk curve for resonant frequency shift relative to the reference.

Fig. 15(a) shows that there is a wide spread in resonant frequency values that occur when measurement uncertainties are considered. If a normal distribution is fit to the data in Fig. 15(b), it results in $\mu = 10.0408$ GHz and $\sigma = 0.3842$ GHz, which correspond to a 95% confidence interval of 9.2723–10.8092 GHz. This average resonant

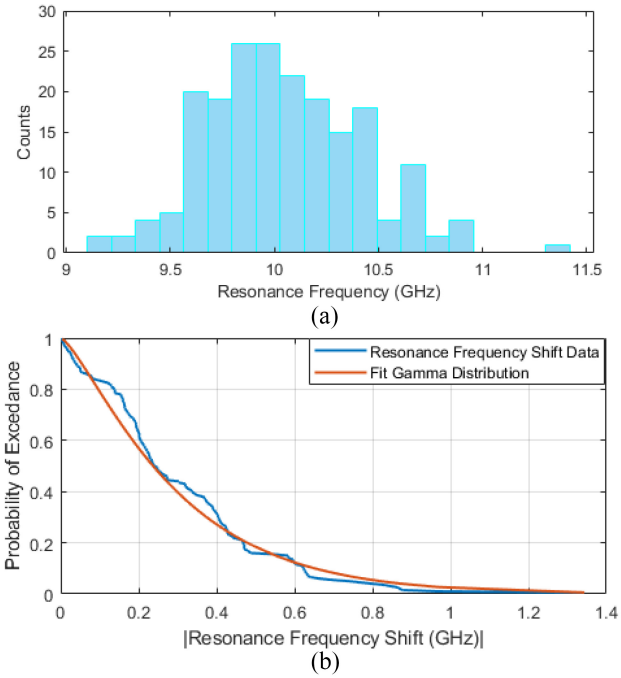

FIGURE 15. Resonant frequency distribution for different pressures when different measurement uncertainties are considered: (a) 5-mm substrate height for misalignment-based uncertainty and (b) 5-mm substrate height for all three measurement uncertainties.

frequency is slightly lower than the reported value for the aligned case (10.0610), which is consistent with the results seen for the other two tags used in this work. Fig. 15(b) shows that there is a relatively high risk for resonant frequency shift (i.e., there is a 61% chance of there being a resonant frequency shift of at least 0.20 GHz, while there was a 37% chance for the Patch tag and a 0% chance for the 4C tag).

This large spread in resonant frequency and high risk for resonant frequency shift would greatly limit the achievable resolution of this sensor since the user would not be able to distinguish whether a resonant frequency value is due to the compression of the sensor or measurement uncertainty. If the misalignment is controlled, especially *dz* translations, the resonant frequency distribution spread could be greatly reduced and the achievable sensing resolution could be improved. These results may also indicate that it could be beneficial to use a different type of resonator that is less sensitive to *dz* translations. Overall, though, it should be noted that due to the small sample size ($n = 200$) of this Monte Carlo simulation, the conclusions that can be drawn from this data are limited. Additionally, the resonant frequency spread could improve to allow for an acceptable sensing resolution if a large enough sample size is used.

V. CONCLUSION

This work examined the effects of three common chipless RFID measurement uncertainties on the responses of two different tags through both local sensitivity analysis and Monte Carlo simulation. In doing so, a general procedure for evaluating measurement uncertainty in chipless RFID

systems was laid out. It was seen that local sensitivity analysis can provide insight into which types of misalignment are the most critical to control during measurement, while the Monte Carlo simulation showed that of the three measurement uncertainties considered (misalignment, clutter, and S_{11} uncertainty), misalignment played the largest role in creating both bit differences and response shape changes, such as magnitude changes and resonant frequency shifts. It was also seen that for this particular measurement configuration (near-field monostatic), S_{11} uncertainty had a larger effect than clutter-based uncertainty. However, this may not be the case for other measurement configurations (e.g., far-field measurements). When all three measurement uncertainties were considered simultaneously, conclusions about the sensing capabilities of each tag could also be made. For the two tags considered, it was seen that the patch tag had a greater resonant frequency variation than the 4C tag, which would result in the patch tag having a lower achievable sensing resolution than the 4C tag. Finally, the simulation results were corroborated with measurement. This showed that the simulation model is conservative and tends to overestimate the measurement uncertainty that is seen in practice. This could potentially be mitigated by developing a less conservative uncertainty propagation model for S_{11} uncertainty. In order to demonstrate the application of the proposed tag performance assessment framework, an example was given in which the analyses were applied to a pressure sensing tag. While this work was done for a monostatic near-field measurement setup, the procedures outlined could also be applied to other chipless RFID measurement approaches, such as far-field and bistatic configurations.

ACKNOWLEDGMENT

The authors would like to thank Dr. Cameron MacKenzie of the Department of Industrial and Manufacturing Systems Engineering (IMSE), Iowa State University for his insight and feedback on the initial modeling that led to this work.

REFERENCES

[1] K. Brinker and R. Zoughi, "Local sensitivity analysis and Monte Carlo simulation to examine the effects of chipless RFID measurement uncertainties—Part I: Misalignment-based uncertainty," *IEEE Open J. Instrum. Meas.*, vol. 1, 2022, Art. no. 8000413.

[2] "Application note: Calculating VNA measurement accuracy." Anritsu. 2008. [Online]. Available: https://www.microwavejournal.com/ext/resources/BGDownload/f/c/Anritsu_Calculating.pdf?1520850769

[3] B. Oldfield, "VNA S11 uncertainty measurement a comparison of three techniques," in *39th ARFTG Conf. Dig.*, vol. 21, Jun. 1992, pp. 86–105, doi: 10.1109/ARFTG.1992.326976.

[4] T. Buber, P. Narang, G. Esposito, S. Padmanabhan, and M. Zeier. "Characterizing uncertainty in S-parameter measurements." Microwave Journal. 2019. [Online]. Available: https://www.microwavejournal.com/articles/32951-characterizing-uncertainty-in-s-parameter-measurements

[5] M. Zeier, D. Allal, and R. Judaschke, "Guidelines on the evaluation of vector network analysers (VNA), version 3.0," EURAMET, Brunswick, Germany, document calibration guide no. 12, 2018.

[6] M. A. Bibile and N. A. Karmakar, "Detection error rate analysis using coloured noise for the movement of chipless RFID tag," in *Proc. Aust. Microw. Symp. (AMS)*, Feb. 2018, pp. 1–2, doi: 10.1109/AUSMS.2018.8346952.

[7] M. Borgese, S. Genovesi, G. Manara, and F. Costa, "Radar cross section of chipless rfID tags and BER performance," *IEEE Trans. Antennas Propag.*, vol. 69, no. 5, pp. 2877–2886, May 2021, doi: 10.1109/TAP.2020.3037800.

[8] M. Borgese, S. Genovesi, G. Manara, and F. Costa, "System level performance in chipless RFID," in *Proc. URSI GASS*, Rome, Italy, 2021, pp. 1–4.

[9] R. D. Errico, "An indoor backscattering channel characterization for UWB passive RFID applications," in *Proc. 6th Eur. Conf. Antennas Propag. (EUCAP)*, Mar. 2012, pp. 1169–1173, doi: 10.1109/EuCAP.2012.6206354.

[10] A. Doukas and G. Kalivas, "Rician K factor estimation for wireless communication systems," in *Proc. Int. Conf. Wireless Mobile Commun. (ICWMC)*, Jul. 2006, p. 69, doi: 10.1109/ICWMC.2006.81.

[11] F. V. D. Wijk, A. Kegel, and R. Prasad, "Assessment of a picocellular system using propagation measurements at 1.9 GHz for indoor wireless communications," *IEEE Trans. Veh. Technol.*, vol. 44, no. 1, pp. 155–162, Feb. 1995, doi: 10.1109/25.350281.

[12] K. R. Brinker and R. Zoughi, "A review of chipless RFID measurement methods, response detection approaches, and decoding techniques," *IEEE Open J. Instrum. Meas.*, vol. 1, 2022, Art. no. 8000331, doi: 10.1109/OJIM.2022.3196746.

[13] K. Brinker and R. Zoughi, "Multi-bit chipless RFID sensing methodology for rotation determination," in *Proc. IEEE Int. Instrum. Meas. Technol. Conf. (I2MTC)*, Dubrovnik, Croatia, May 2020, pp. 1–6.

[14] K. Brinker and R. Zoughi, "Tunable chipless RFID pressure sensor utilizing additive manufacturing," in *Proc. IEEE Int. Instrum. Meas. Technol. Conf. (I2MTC)*, Ottawa, Canada, May 2022, pp. 1–6.

[15] O. Rance, N. Barbot, and E. Perret, "Monte Carlo simulation for chipless RFID orientation sensor," in *Proc. IEEE Int. Symp. Antennas Propag. North Amer. Radio Sci. Meeting*, Jul. 2020, pp. 1199–1200, doi: 10.1109/IEEECONF35879.2020.9329985.

[16] K. Brinker and R. Zoughi, "Chipless RFID tags as microwave sensors for delamination detection in layered structures," in *Proc. IEEE Int. Instrum. Meas. Technol. Conf. (I2MTC)*, May 2021, pp. 1–6, doi: 10.1109/I2MTC50364.2021.9459795.